

RESEARCH ARTICLE

Parametric topology optimization with multiresolution finite element models

Vahid Keshavarzzadeh¹  | Robert M. Kirby^{1,2} | Akil Narayan^{1,3}

¹Scientific Computing and Imaging Institute, The University of Utah, Salt Lake City, Utah

²School of Computing, The University of Utah, Salt Lake City, Utah

³Department of Mathematics, The University of Utah, Salt Lake City, Utah

Correspondence

Vahid Keshavarzzadeh, Scientific Computing and Imaging Institute, The University of Utah, Salt Lake City, UT 84112.

Email: vkeshava@sci.utah.edu

Funding information

Army Research Laboratory (ARL), Grant/Award Number: W911NF-12-2-0023; Air Force Office of Scientific Research, Grant/Award Number: FA9550-15-1-0467; Defense Advanced Research Projects Agency through the Enabling Quantification of Uncertainty in Physical Systems (EQUIPS), Grant/Award Number: N660011524053; National Science Foundation Division of Mathematical Sciences, Grant/Award Number: 1720416

Summary

We present a methodical procedure for topology optimization under uncertainty with multiresolution finite element (FE) models. We use our framework in a bifidelity setting where a coarse and a fine mesh corresponding to low- and high-resolution models are available. The inexpensive low-resolution model is used to explore the parameter space and approximate the parameterized high-resolution model and its sensitivity, where parameters are considered in both structural load and stiffness. We provide error bounds for bifidelity FE approximations and their sensitivities and conduct numerical studies to verify these theoretical estimates. We demonstrate our approach on benchmark compliance minimization problems, where we show significant reduction in computational cost for expensive problems such as topology optimization under manufacturing variability, reliability-based topology optimization, and three-dimensional topology optimization while generating almost identical designs to those obtained with a single-resolution mesh. We also compute the parametric von Mises stress for the generated designs via our bifidelity FE approximation and compare them with standard Monte Carlo simulations. The implementation of our algorithm, which extends the well-known 88-line topology optimization code in MATLAB, is provided.

KEYWORDS

3D topology optimization, bifidelity error estimate, manufacturing variability, multiresolution finite elements, parametric topology optimization

1 | INTRODUCTION

Topology optimization is a systematic design framework for the distribution of given material resources within a specified spatial domain to achieve maximum stiffness. This technique spawns from a seminal paper by Bendsoe and Kikuchi¹ in which the structure layout, instead of structure boundaries as done in shape optimization, is optimized. Since then, in addition to solid mechanics,² topology optimization has been developed and extended to various fields, such as heat conduction, fluid dynamics, and multi-physics simulations.³⁻⁷ A majority of existing works focus on deterministic analysis and optimization for such designs. However, the design performance varies due to inherent uncertainties in different parameters, such as loading, boundary conditions, material properties, and geometry.

This performance deficiency can be overcome by incorporating uncertainty analysis in the optimization process; in robust design optimization (RDO),⁸⁻¹⁴ the performance variation is minimized, and in reliability-based design

optimization (RBDO),¹⁵⁻¹⁷ the failure probability is constrained. Computational complexity is the outstanding challenge in these approaches due to requiring a considerable number of expensive simulations to capture variations in parameter/stochastic space. Multiresolution and multifidelity finite element (FE) models have been used in a number of studies to enhance the computational efficiency of topology optimization.¹⁸⁻²² These multiresolution/multifidelity topology optimization approaches are explored within a deterministic framework, ie, when the focus is only on a limited number of deterministic simulations throughout different mesh resolutions.

In this work, we adopt a different perspective in multiresolution topology optimization and use coarse and fine FE meshes within a parametric/stochastic framework. We use the inexpensive low-resolution model to traverse the parameter space and use that information to predict the stochastic response and sensitivity of the expensive high-resolution model. In this way, stochastic analysis is primarily performed via a low-resolution model, which drastically decreases the computational complexity. Similar multifidelity approaches for acceleration of parametric studies have been recently reported in different areas, such as molecular dynamics simulations, orbit-state uncertainty propagation, and combustion and turbulence modeling.²³⁻²⁶

We provide theoretical discussions that motivate the success of our approach, and we show via numerical examples that using a low-resolution model that is far coarser than necessary for any meaningful physical predictive power is able to give substantial insight into parametric variation. Our method is nonintrusive, ie, it is implemented with minimal modification to the existing codes for topology optimization. We present our approach in the context of a generic density-based topology optimization; however, it is similarly applicable to a level set-based method. The implementation of our approach, which is the extension of “Efficient topology optimization in MATLAB using 88 lines of code,”²⁷ is provided in the work of Keshavarzzadeh.²⁸ We also provide error bounds for the bifidelity construction of compliance and its sensitivity, which serves as a certificate for the convergence of our parametric topology optimization approach. We provide numerical results to delineate the error estimate for compliance and its sensitivity.

This paper is organized as follows. Section 2 briefly describes the topology optimization including its deterministic and parametric forms. The details of our multiresolution approach are presented in Section 3. Section 4 presents numerical results for topology optimization under loading and manufacturing variability in conjunction with computational cost studies. Finally, Section 5 contains concluding remarks.

2 | TOPOLOGY OPTIMIZATION

2.1 | Notation and setup

We use bold characters to denote matrices, vectors, and multivariate quantities, eg, \mathbf{x} indicates a vector of variables in the domain of a multivariate function. We denote sets with uppercase letters, eg, \mathbf{P} is a set of sample parameters.

In this paper, we mainly focus on parameterized elastostatic problems with the general form of

$$\begin{aligned}\mathcal{L}\{\mathbf{u}(x, \mathbf{p})\} &= f(x, \mathbf{p}), & x \in \Omega, & \mathbf{p} \in \mathbf{P} \\ \mathbf{u}(x, \mathbf{p}) &= \mathbf{u}_b(\mathbf{p}), & x \in \partial\Omega, & \mathbf{p} \in \mathbf{P},\end{aligned}\tag{1}$$

where \mathcal{L} denotes a linear operator, which will be replaced by the generic FE global stiffness matrix shortly, Ω is the spatial domain, and the parameter $\mathbf{p} \in \mathbf{P}$ later will be treated as random variables. We consider two models: low-resolution model $\mathbf{u}^L : \mathbf{P} \rightarrow \mathbf{U}^L$ corresponding to the coarse mesh and high-resolution model $\mathbf{u}^H : \mathbf{P} \rightarrow \mathbf{U}^H$ corresponding to the fine mesh. Here, \mathbf{U}^L and \mathbf{U}^H are Hilbert spaces equipped with inner products $\langle \cdot, \cdot \rangle^L, \langle \cdot, \cdot \rangle^H$, respectively. For example, if \mathbf{U}^L is finite dimensional and two elements a and b of this space are represented as coordinates in the vectors \mathbf{a} and \mathbf{b} , then one way to define an inner product is

$$\langle a, b \rangle^L = \frac{\mathbf{a}^T \mathbf{b}}{\dim \mathbf{a}},\tag{2}$$

where \dim denotes dimension or the size of a vector, and $\dim \mathbf{a} = \dim \mathbf{b}$. We hereafter assume that \mathbf{U}^L and \mathbf{U}^H are finite dimensional, respectively of dimensions N_{dof}^L and N_{dof}^H . Due to our coarse mesh/fine mesh assumptions, we have $N_{\text{dof}}^L < N_{\text{dof}}^H$, and typically, $N_{\text{dof}}^L \ll N_{\text{dof}}^H$.

In this paper, we seek to find accurate approximations to the high-resolution model \mathbf{u}^H by using the low-resolution model \mathbf{u}^L in the parameter space. We use hat notation to denote approximations, eg, $\hat{\mathbf{u}}$ is an approximation to \mathbf{u} . The low-resolution solution can be computed on a collection of parametric samples $\Gamma_N = \{p_1, p_2, \dots, p_N\} \subset \mathbf{P}$ in a relatively

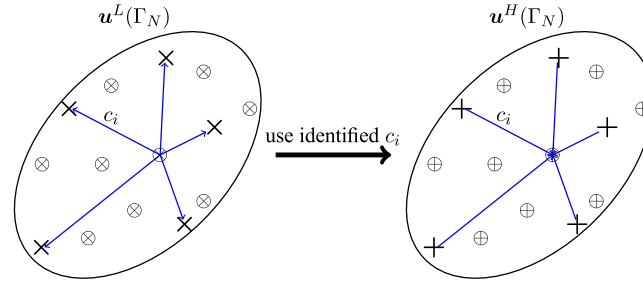


FIGURE 1 Schematic representation for bifidelity construction of parametric finite element solutions. The low- and high-resolution important samples are denoted by \times and $+$. To estimate the high-resolution samples on unknown locations in parameter space \oplus , we use the identified coefficients c_i from the low-resolution sample space [Colour figure can be viewed at wileyonlinelibrary.com]

small amount of time. We denote the collection of these solution samples and their span as

$$\begin{aligned} \mathbf{u}^L(\Gamma_N) &= \{\mathbf{u}^L(p_1), \mathbf{u}^L(p_2), \dots, \mathbf{u}^L(p_N)\}, \\ \mathbf{U}_{\Gamma_N}^L &= \text{span } \mathbf{u}^L(\Gamma_N) = \text{span } \{\mathbf{u}^L(p_1), \mathbf{u}^L(p_2), \dots, \mathbf{u}^L(p_N)\} \end{aligned} \quad (3)$$

and use similar notation for \mathbf{u}^H . The term span above denotes the subspace that is formed with any linear combination of the solution samples $\mathbf{u}^L(p_i)$. We view the collection of samples as a matrix, eg, $\mathbf{u}^L(\Gamma_N) = [\mathbf{u}^L(p_1) \mathbf{u}^L(p_2) \dots \mathbf{u}^L(p_N)]_{N_{\text{dof}}^L \times N}$ in our matrix computations.

Once we compute the low-resolution FE responses on the entire sample space, we find important samples and identify coefficients that “relate” the important samples to the rest of the samples in Γ_N . Computing the high-resolution important samples, which are few, we then use the identified coefficients to estimate the high-resolution responses on the rest of the samples. Figure 1 shows the schematic representation of this bifidelity construction.

2.2 | Deterministic optimization

Topology optimization in its original form is a constrained optimization problem that minimizes compliance subject to a volume constraint. To find compliance, structural analysis is typically performed via the FE method. We consider density-based topology optimization in which the design space is characterized with element volume fractions. The optimization problem after FE discretization is stated as

$$\begin{aligned} \min_{\boldsymbol{\rho}} C(\boldsymbol{\rho}) &= \mathbf{U}^T \mathbf{F} \\ \text{subject to } V(\boldsymbol{\rho}) &\leq \bar{V} \\ \mathbf{K}(\boldsymbol{\rho}) \mathbf{U}(\boldsymbol{\rho}) &= \mathbf{F}(\boldsymbol{\rho}) \\ \rho_{\min} &\leq \boldsymbol{\rho} \leq 1, \end{aligned}$$

where \mathbf{K} , \mathbf{U} , and \mathbf{F} denote the global FE stiffness matrix, the displacement vector, and the force vector, respectively, $\boldsymbol{\rho}$ is the vector of element volume fractions, C is the compliance, V is the volume, and $0 < \rho_{\min} \ll 1$ is the lower bound for the volume fractions.

We process the design variables throughout the optimization in two ways: (i) we impose a minimum length scale by using the filtered volume fraction to generate a well-posed topology optimization formulation, and (ii) we use Heaviside thresholding to generate more distinct interfaces and to model geometric variabilities.

The filtered volume fractions $\hat{\rho}$ are expressed via the cone kernel K_F , ie,

$$\hat{\rho}(x_i) = \frac{\sum_{j=1}^n K_F(x_i, x_j) \rho(x_j)}{\sum_{j=1}^n K_F(x_i, x_j)}, \quad i = 1, \dots, n, \quad (4)$$

where

$$K_F(x_i, x_j) = \begin{cases} r_{\min} - |x_i - x_j|, & \text{if } |x_i - x_j| \leq r_{\min} \\ 0, & \text{if } |x_i - x_j| > r_{\min}. \end{cases} \quad (5)$$

In these expressions, r_{\min} and x_i denote the filter radius and the element i centroid.²⁹ Ideally, the Heaviside step function is used to threshold the filtered volume fractions to 0 and 1, eg, $\bar{\rho} = H(\hat{\rho} - 0.5)$. However, to make the thresholding possible for sensitivity analysis and optimization, a smooth approximation of a step function

$$\bar{\rho} = H_{\beta, \tau}(\hat{\rho}) = \frac{\tanh(\beta\tau) + \tanh(\beta(\hat{\rho} - \tau))}{\tanh(\beta\tau) + \tanh(\beta(1 - \tau))} \quad (6)$$

is used. In this approximation, β controls the smoothness of transition, and $\tau \in [0, 1]$ serves as the threshold, ie, $\lim_{\beta \rightarrow \infty} H_{\beta, \tau}(x) = H(x - \tau)$ pointwise for all $x \neq \tau$. We use the latter parameter τ to vary the boundary, ie, geometry of the structure. It will be used as an uncertain parameter in our numerical examples to model the geometric tolerances, which may arise in the manufacturing process.

Finally, we use the solid isotropic material with penalization method to penalize intermediate volume fractions.^{30,31} As such, we compute the global stiffness matrix \mathbf{K} by using the processed (thresholded-filtered) volume fractions $\bar{\rho}$, ie,

$$\mathbf{K} = \sum_{i=1}^n \bar{\rho}_i^t \mathbf{K}_i, \quad (7)$$

where n is the number of elements, $t = 3$ is the penalization parameter, and \mathbf{K}_i is the nominal element i stiffness matrix.

2.3 | Parametric optimization

We consider uncertainties in loading and geometry in our topology optimization statement problem by introducing the parameter \mathbf{p} in loading and structure stiffness, ie,

$$\mathbf{K}(\boldsymbol{\rho}, \mathbf{p})\mathbf{U}(\boldsymbol{\rho}, \mathbf{p}) = \mathbf{F}(\boldsymbol{\rho}, \mathbf{p}), \quad \mathbf{p} \in \mathbf{P}, \quad (8)$$

where the parameters are treated as random variables. Since \mathbf{U} and, subsequently, \mathbf{C} are therefore random, we restate the optimization problem with a quantity of interest Q , which depends on statistical moments of \mathbf{C} , as follows:

$$\begin{aligned} \min_{\boldsymbol{\rho}} Q(\lambda) &= \mu(\boldsymbol{\rho}) + \lambda\sigma(\boldsymbol{\rho}) \\ \text{subject to } E[V(\boldsymbol{\rho})] &\leq \bar{V} \\ \rho_{\min} &\leq \boldsymbol{\rho} \leq 1, \end{aligned} \quad (9)$$

where μ and σ are the mean and standard deviation of the compliance C (cf Section 3.4), and λ is a weight factor associated with the standard deviation. We note that this formulation is pertinent to the case of geometric uncertainty where we consider the expected value for volume. In addition to the above RDO problem, we solve RBDO by constraining the probability of failure

$$\begin{aligned} \min_{\boldsymbol{\rho}} E[V(\boldsymbol{\rho})] \\ \text{subject to } \Pr[C(\boldsymbol{\rho}) > \bar{C}] &\leq \delta_{P_f} \\ \rho_{\min} &\leq \boldsymbol{\rho} \leq 1, \end{aligned} \quad (10)$$

where $C(\boldsymbol{\rho}) > \bar{C}$ is a condition defining failure events, and δ_{P_f} is the tolerance for failure.

We consider a Karhunen-Loeve expansion to model uncertainties in both distributed load and spatial threshold parameters τ . We assume a covariance function

$$\mathbf{R}_{x x'} = \exp\left(-\frac{\|x - x'\|_2^2}{2l_c^2}\right), \quad (11)$$

where $\|x - x'\|_2$ is the Euclidean distance between locations x and x' and l_c is the correlation length. We discretize this covariance function with x and x' as (i) the FE centroids in the case of spatial threshold and (ii) the FE nodes that are under the influence of load in the case of distributed load to obtain the correlation matrix \mathbf{R} . We use n_M first eigenvalue-eigenvector pairs $(\eta_i, \boldsymbol{\gamma}_i)$ of the covariance matrix to generate the KL decomposition of a zero-mean process as

$$Z(x, \mathbf{p}) = \gamma_0 + \sum_{i=1}^{n_M} \sqrt{\eta_i} \boldsymbol{\gamma}_i(x) \varphi_i(\mathbf{p}), \quad (12)$$

where φ_i are uniform random variables and $\boldsymbol{\gamma}_i$ are eigenvectors, and $\gamma_0 > 0$ is a constant that is chosen to ensure a positive distributed load and avoid erratic distributions. We also post-process the random field Z in the case of a spatial

threshold since Z is not necessarily in the desirable range $Z \notin [0, 1]$. In this case, to generate a value in the range $[0, 1]$, we transform Z into its cumulative distribution function (CDF), ie, $Z \leftarrow \Phi(Z) \in [0, 1]$, where Φ is the CDF of Z . For a detailed discussion of this transformation, see the work of Keshavarzzadeh et al.¹² We finally use an affine map $\tau_i = a_1 Z(p_i) + a_2$ for suitable constants a_1 and a_2 to map values of Z to an appropriate range.

The random processes are evaluated on Monte Carlo (MC) samples or quadrature points $Z(x, p_i)$, where each sample corresponds to a parametric load $\mathbf{F}(p_i)$ or stiffness matrix $\mathbf{K}(p_i)$. For a given FE resolution, the parametric analysis is summarized as follows.

- Loading uncertainty: for each parameter p_i , solve $\mathbf{K}\mathbf{U} = \mathbf{F}(p_i)$ to find the parametric $\mathbf{U}(p_i)$, parametric compliance $C(p_i) = \mathbf{U}(p_i)^T \mathbf{K}\mathbf{U}(p_i)$, and parametric compliance sensitivity $\partial C(p_i)/\partial \rho = \mathbf{\Lambda}(p_i)^T (\partial \mathbf{K}(\rho)/\partial \rho) \mathbf{U}(p_i)$, where $\mathbf{\Lambda} = -\mathbf{U}$ is the adjoint sensitivity solution for compliance.
- Geometric uncertainty: solve $\mathbf{K}(p_i)\mathbf{U} = \mathbf{F}$ for each parameter p_i to find the parametric displacement, compliance, and its sensitivity similarly to loading uncertainty. Note that, in this case, the derivative of the stiffness matrix is dependent on the parameter.

Remark 1. In the case of loading uncertainty, it is possible to compute the response only for the principal KL modes and use superposition to find the total response since the structure is linear. However, as we mainly perform parametric analysis on the coarse mesh, solving the FE system for a large number of samples does not pose a significant challenge.

3 | MULTIREOLUTION FRAMEWORK

Our multiresolution topology optimization framework has four major components summarized below. The detailed description of each component is provided in the following.

- Translation: given high-resolution element density and parametric quantities, translate these data to the low-resolution FE model (cf Section 3.1).
- Important samples: perform parametric analysis with the low-resolution FE model on a large number of samples and determine important samples (cf Section 3.2).
- Bifidelity construction: compute interpolative coefficients in the parametric low-resolution space and use those to estimate the parametric high-resolution response and sensitivities (cf Section 3.3).
- Primal and sensitivity analyses: compute statistical moments of compliance and their sensitivity and feed to the optimizer (cf Section 3.4).

3.1 | Transition between high- and low-resolution models

Our ultimate goal is to produce a design with fine resolution. The optimization progresses with the fine-resolution model; however, the information from the fine resolution should be translated to the low-resolution model where the main FE computations are performed. In particular, the KL model $Z(x, p_i)$ and densities ρ associated with the fine mesh should be translated to the low-resolution mesh. The translation of the KL model is trivial since it can be consistently generated for two resolutions by considering coarse and fine coordinates in the generation of the covariance matrix. Similarly, the KL modes for the low-resolution mesh can be interpolated from the high-resolution mesh. In our numerical examples, for one-dimensional translation such as loading uncertainty in Example 4.1, we use a linear interpolation between high and low resolutions. That is, having high-resolution data on a line, we use linear interpolation to get data on coarse increments. For two-dimensional translation such as manufacturing uncertainty in Example 4.2, we use the averaging approach, which is described below.

To translate densities from the fine model to the coarse model, we use simple averaging, as follows:

$$\rho^L = \frac{1}{n_H} \sum_{i=1}^{n_H} \rho_i^H, \quad (13)$$

where n_H is the number of fine-mesh elements that can be placed in a coarse mesh considering that we only use standard square elements. For example, four fine-mesh elements with size $dx = dy = 0.5$ cover a coarse element with

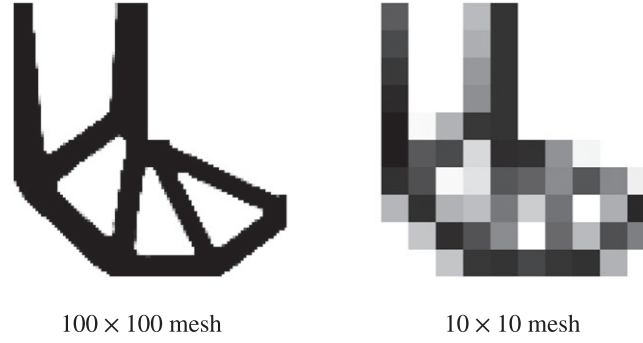


FIGURE 2 Transformation of density ρ from high resolution (left) to low resolution (right). Each element in the right mesh is obtained by averaging the densities of a 10×10 cell in the left mesh

$dx = dy = 1$. Figure 2 shows the transformation of high-resolution densities (100×100 mesh) to low-resolution densities (10×10 mesh).

3.2 | Interpolation nodes

Having the density and parameters associated with the low-resolution mesh, a large number of simulations N is performed. A crucial step is to determine $n \ll N$ points at which the fine-resolution finite element analysis (FEA) will be performed. We determine important samples based on the fact that the span produced by the basis vectors $\{\mathbf{u}^L(k_1), \mathbf{u}^L(k_2), \dots, \mathbf{u}^L(k_n)\}$ gets as close as possible to the span $\mathbf{U}_{\Gamma_N}^L$, which includes N samples. To quantify closeness, we define the standard distance between a function and a subspace as

$$d^L(x, Y) = \inf_{y \in Y} \|x - y\|^L = \|(I - P_Y)x\|^L, \quad (14)$$

where P_Y is the orthogonal projection operator onto a subspace Y , and I is the identity operator.

The selection of important samples from a sample pool to minimize the above distance is a complex combinatorial problem. Typically, greedy procedures, which are computationally tractable, are adopted for such problems, eg, in the reduced basis methods.³² In particular, one may initialize the procedure with a trivial subspace $\Gamma_0 = \{\}$ and iteratively add samples to the set to maximize the distance between the newly added sample and the existing span, ie,

$$p_n = \arg \max_{p \in \Gamma_N} d^L(\mathbf{u}^L(p), \mathbf{U}^L(\Gamma_{n-1})), \quad \Gamma_n = \Gamma_{n-1} \cup \{p_n\}. \quad (15)$$

We note that the distance is maximized such that the newly added samples cover more linearly independent directions in the span. We also note that the number of subsamples $n \ll N$ is determined based on our computational budget. Naturally using more samples results in more accurate reconstruction of unknown samples in parameter space, as long as the number of samples does not exceed the numerical rank of $\mathbf{u}^L(\Gamma_N)$.

This greedy procedure can be performed via standard numerical linear algebra operations, as discussed in the work of Narayan et al.³³ In the aforementioned work, three different linear algebraic choices, namely, (i) column-pivoting QR decomposition, (ii) full-pivoting LU decomposition, and (iii) pivoted Cholesky decomposition, are discussed. We adopt the column-pivoting QR decomposition in this work and use the pivot information to select the n important samples of \mathbf{U}^L . The pivot contains the index of columns such that the first n columns are linearly independent.³⁴

We only need the integer-valued pivot in this paper; however, given a matrix $\mathbf{A} \in \mathbb{R}^{m \times n}$ with $m > n$, one can use the upper-triangular matrix \mathbf{R} from the output of the QR decomposition (see equation 5.1.5 in the work of Golub and Van Loan³⁴) to compute \mathbf{Q} . It can then be verified that $\mathbf{A}\mathbf{\Pi} = \mathbf{Q}\mathbf{R}$, where $\mathbf{\Pi}$ is the $n \times n$ permutation matrix that contains the pivot indices. Equivalently, the pivoted QR factorization can be performed via a built-in function in MATLAB denoted by qr , which we use in our numerical examples.

3.3 | Bifidelity construction

We now have N low-resolution FE solutions and have identified n parameters at which we perform high-resolution simulations $\{\mathbf{u}^H(p_i)\}_{i=1}^n$. We aim to find an approximation to $\mathbf{u}^H(p_i)$ on unknown samples $p_i \in \Gamma_{N-n}$.

Having \mathbf{u}^L on the entire sample space, it is possible to construct the best parametric approximation to the low-resolution solutions $\{\mathbf{u}^L(p_i)\}_{i=n+1}^N$ as a function of important samples $\{\mathbf{u}^L(p_i)\}_{i=1}^n$ and subsequently use the same approximations

to estimate parametric high-resolution solutions $\{\hat{\mathbf{u}}^H(p_i)\}_{i=n+1}^N$. Precisely, the best approximation is defined such that $\|\hat{\mathbf{u}}^L(p_i) - \mathbf{u}^L(p_i)\|$, $\forall p_i \in \{p_{n+1}, \dots, p_N\}$ is minimized. This can be expressed as

$$\langle \hat{\mathbf{u}}^L(p_i), \gamma(p) \rangle^L = \langle \mathbf{u}^L(p_i), \gamma(p) \rangle^L \quad \forall \gamma \in \mathbf{U}^L(\Gamma_n), \quad \hat{\mathbf{u}}^L(p_i) \in \mathbf{U}^L(\Gamma_n), \quad (16)$$

which is equivalent to a projection of $\{\mathbf{u}^L(p_i)\}_{i=n+1}^N$ onto the space $\mathbf{U}^L(\Gamma_n)$ denoted by $\mathbf{P}_{\mathbf{U}^L(\Gamma_n)}$, ie,

$$\mathbf{I}_L^L(\mathbf{u}^L(\Gamma_n)) := \hat{\mathbf{u}}^L(p_i) = \sum_{j=1}^n c_j \mathbf{u}^L(p_j), \quad (17)$$

where we have defined the interpolation operator \mathbf{I}_L^L using coefficients c_j obtained from low-resolution conditions (16) to approximate low-resolution solutions on $\{p_i\}_{i=n+1}^N$.

The linear algebraic version of (16) is

$$\mathbf{G}^L \mathbf{c}^L = \mathbf{f}^L, \quad (18)$$

where the low-resolution Gramian \mathbf{G}^L and \mathbf{f}^L are expressed as

$$\begin{aligned} \mathbf{G}_{ij}^L &= \langle \mathbf{u}^L(p_i), \mathbf{u}^L(p_j) \rangle^L, \quad \forall p_i, p_j \in \{p_1, \dots, p_n\}, \\ \mathbf{f}_i^L &= (f_i^L)_{1 \leq i \leq n}, \quad f_i^L = \langle \mathbf{u}^L(p_i), \mathbf{u}^L(p_j) \rangle^L, \quad p_j \in \{p_{n+1}, \dots, p_N\}. \end{aligned} \quad (19)$$

Note that the Gramian \mathbf{G}^L is constructed once for all important samples; however, the right-hand side \mathbf{f}^L is computed for every parameter $\{p_i\}_{i=n+1}^N$ individually. Therefore, this analysis yields $N - n$ coefficient vectors \mathbf{c} . We also note that solving the linear system (18) is not challenging since the size of \mathbf{G}^L is small.

Upon finding the coefficients \mathbf{c} , we estimate the higher-resolution solutions $\{\mathbf{u}^H(p_i)\}_{i=n+1}^N$ by a lifting procedure, ie,

$$\hat{\mathbf{u}}^H(p_i) = \mathbf{I}_L^H(\mathbf{u}^L(\Gamma_n)) := \sum_{j=1}^n c_j \mathbf{u}^H(p_j). \quad (20)$$

We now have the high-resolution response on the entire sample space, ie, we have $\mathbf{U}^H(\Gamma_N) = \{\mathbf{u}^H(p_1), \dots, \mathbf{u}^H(p_n), \hat{\mathbf{u}}^H(p_{n+1}), \dots, \hat{\mathbf{u}}^H(p_N)\}$. Having the high-resolution response, which is equivalent to the adjoint solution, we compute approximations \hat{C} and $\partial \hat{C} / \partial \boldsymbol{\rho}$ to the compliance and its sensitivity for the sample space Γ_N : $\{\hat{C}(p_1), \partial \hat{C}(p_1) / \partial \boldsymbol{\rho}, \dots, \hat{C}(p_N), \partial \hat{C}(p_N) / \partial \boldsymbol{\rho}\}$ as discussed in Section 2.3.

Algorithm 1 summarizes the steps in bifidelity construction.

Algorithm 1 Bifidelity construction

- 1: Given $\mathbf{u}^L(\Gamma_N)$ and important samples $\{p_i\}_{i=1}^n$ compute $\{\mathbf{u}^H(p_i)\}_{i=1}^n$
 - 2: Form Gramian $\mathbf{G}_{ij}^L = \langle \mathbf{u}^L(p_i), \mathbf{u}^L(p_j) \rangle^L$ once $\forall p_i, p_j \in \{p_1, \dots, p_n\}$ using Equation (19)
 - 3: Compute the right-hand side in (18) for every parameter $\{p_i\}_{i=n+1}^N$ using Equation (19)
 - 4: Compute coefficients \mathbf{c}^L in (18)
 - 5: Form the interpolants for \mathbf{u}^H , ie, $\hat{\mathbf{u}}^H = \sum_{i=1}^n c_i \mathbf{u}^H(p_i)$
 - 6: Compute compliance and its sensitivity $\{C(p_i), \partial C(p_i) / \partial \boldsymbol{\rho}\}_{i=1}^N$ associated with the response samples $\mathbf{U}^H(\Gamma_N) = \{\mathbf{u}^H(p_1), \dots, \mathbf{u}^H(p_n), \hat{\mathbf{u}}^H(p_{n+1}), \dots, \hat{\mathbf{u}}^H(p_N)\}$
-

3.4 | Primal and sensitivity analyses

To compute statistical moments in the optimization problem in Section 2.2, we use either a quadrature rule or MC integration. In either case, we compute N higher-resolution samples (or approximations to them as described previously) and subsequently compute μ and σ

$$\begin{aligned} \mu &= E[C] = \sum_{i=1}^N C(p_i) w_i \\ \sigma &= \sqrt{E[(C - \mu)^2]} = \sqrt{\sum_{i=1}^N C^2(p_i) w_i - \mu^2}, \end{aligned} \quad (21)$$

where $w_i = 1/N$ in the case of MC integration. The sensitivity of statistical moments is computed similarly, ie,

$$\begin{aligned}\frac{\partial \mu}{\partial \rho} &= \sum_{i=1}^N \frac{\partial C(p_i)}{\partial \rho} w_i \\ \frac{\partial \sigma}{\partial \rho} &= \frac{1}{\sigma} \left(\sum_{i=1}^N C(p_i) \frac{\partial C(p_i)}{\partial \rho} w_i - \mu \frac{\partial \mu}{\partial \rho} \right),\end{aligned}\quad (22)$$

where $\partial C(p_i)/\partial \rho$ is readily available from the high-resolution displacement $\mathbf{u}^H(p_i)$.

To compute the probability of failure and its sensitivity, we adopt the approach in the works of Keshavarzzadeh et al,^{11,12} ie, we compute

$$\begin{aligned}\Pr[C > \bar{C}] &= \frac{1}{N} \sum_{i=1}^N H(C(p_i) - \bar{C}) \\ &= \frac{n_{C > \bar{C}}}{N},\end{aligned}\quad (23)$$

where $n_{C > \bar{C}}$ denotes the number of MC samples that satisfy $C > \bar{C}$ and H is the Heaviside function. To compute the sensitivity, we replace H with its smooth approximation

$$H_\varepsilon(x) = \frac{1}{2} \left(\tanh\left(\frac{x}{\varepsilon}\right) + 1 \right), \quad (24)$$

where $\varepsilon > 0$ is a small number that controls the width of the 0-to-1 transition such that $H(x) = \lim_{\varepsilon \rightarrow 0} H_\varepsilon(x)$. Taking the derivative with respect to ρ yields the sensitivity

$$\frac{\partial \Pr[C > \bar{C}]}{\partial \rho} = \frac{1}{2\varepsilon N} \sum_{i=1}^N \frac{\partial C(p_i)}{\partial \rho} \left(1 - \tanh^2\left(\frac{C(p_i) - \bar{C}}{\varepsilon}\right) \right). \quad (25)$$

We use $\varepsilon = 0.01\sigma(\rho)$ (cf Equation (9)) in our numerical simulations according to the work of Keshavarzzadeh et al.¹¹ As mentioned, we need high-resolution MC samples to estimate the probability of failure and its sensitivity. The bi-resolution strategy in this paper significantly facilitates the approximation to high-resolution samples, as will be shown in the numerical examples.

Algorithm 2 summarizes the steps and Figure 3 depicts the flowchart for the bifidelity topology optimization for compliance minimization.

Algorithm 2 Bifidelity topology optimization

- 1: Given design iterate ρ in the high-resolution mesh, transform it to a low-resolution mesh via Equation (13)
 - 2: Perform low-resolution FEA on N samples where N is determined from a Monte Carlo analysis or a quadrature rule and find N displacement vectors $\{\mathbf{u}^L(p_i)\}_{i=1}^N$
 - 3: Perform pivoted QR decomposition on \mathbf{U}^L to select $n \ll N$ important samples $\{p_i\}_{i=1}^n$ (cf Section 3.2)
 - 4: Compute low-resolution Gramian and use it to find interpolative coefficients $\{c_i^L\}_{i=1}^{N-n}$ associated with the remaining samples (cf Equations (18) and (19))
 - 5: Perform high-resolution FEA on n samples to find displacement vectors $\{\mathbf{u}^H(p_i)\}_{i=1}^n$
 - 6: Use interpolative coefficients $\{c_i\}_{i=1}^{N-n}$ of Step 4 to estimate the displacement on the remaining $N - n$ high-resolution samples $\{\hat{\mathbf{u}}^H(p_i)\}_{i=1}^{N-n}$
 - 7: Compute compliance and its sensitivity $\{C(p_i), \partial C(p_i)/\partial \rho\}_{i=1}^N$ associated with the displacements $\left\{ \{\mathbf{u}^H(p_i)\}_{i=1}^n, \{\hat{\mathbf{u}}^H(p_i)\}_{i=1}^{N-n} \right\}$
 - 8: For robust design optimization, compute μ and σ and their sensitivities via Equations (21) and (22), and for reliability-based design optimization, compute probability of failure and its sensitivity via Equations (23) and (25)
 - 9: Feed the information from the previous step to gradient-based optimizer and get the new high-resolution design iterate, go back to Step 1
-

Parametric Topology Optimization with Multi-Resolution FE Models

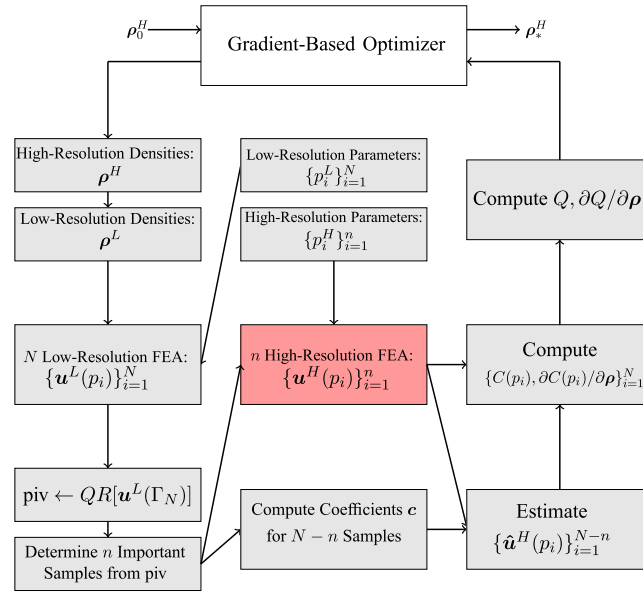


FIGURE 3 Flowchart of the parametric topology optimization with multi-resolution finite element (FE) models. Note that the low- and high-resolution parameters are obtained once before the inception of optimization. FEA, finite element analysis [Colour figure can be viewed at wileyonlinelibrary.com]

3.5 | Error estimate for bifidelity compliance and its sensitivity

In this section, we first provide theoretical explanations as to why this particular multifidelity approximation is effective. We then derive an estimate for compliance and its sensitivity, which bounds the discrepancy between the bi-resolution and high-resolution approximations. Before beginning the discussion, we introduce some additional notation. Similar to Equation (19), let

$$\begin{aligned}
 G_{ij}^H &= \langle \mathbf{u}^H(p_i), \mathbf{u}^H(p_j) \rangle^H, \quad \forall p_i, p_j \in \{p_1, \dots, p_n\} \\
 f_i^H &= \langle \mathbf{u}^H(p_i), \mathbf{u}^H(p_j) \rangle^H, \quad p_j \in \{p_{n+1}, \dots, p_N\} \\
 \mathbf{P}_{\mathbf{U}_n^H} \mathbf{u}^H(p_i) &= \sum_{j=1}^n c_j^H \mathbf{u}^H(p_j)
 \end{aligned} \tag{26}$$

be the high-resolution Gramian, forcing term, and interpolator. The high-fidelity coefficients \mathbf{c}^H can then be obtained from $\mathbf{G}^H \mathbf{c}^H = \mathbf{f}^H$.

The first error analysis for this procedure is reported in the work of Narayan et al.³³ In this paper, the authors develop an error estimate by assuming enough proximity for low- and high-resolution Gramians \mathbf{G}^L and \mathbf{G}^H (cf theorem 4.4 in the work of Narayan et al.³³). This analysis is, unfortunately, unwieldy and not easily computable. Recently, more practical criteria for this multifidelity approximation are given in the work of Hampton et al.³⁵ We report the main theorem of Hampton et al.³⁵ at this juncture.

Theorem 1. *Let the low- and high-resolution Gramians be denoted by \mathbf{G}^L and \mathbf{G}^H , and let $\epsilon(\kappa) = \lambda_{\max}(\mathbf{G}^H - \kappa \mathbf{G}^L)$, where λ_{\max} denotes the largest eigenvalue of the matrix for some $\kappa \geq 0$. Furthermore, let σ_k denote the k th singular value of matrix \mathbf{U}^L , then the bifidelity approximation of high-resolution response is bounded via*

$$\|\hat{\mathbf{u}}^H - \mathbf{u}^H\| \leq \left[1 + \sqrt{n} + \frac{N_{\text{dof}}^L \max_{i \in [1, \dots, n]} \|\hat{\mathbf{u}}^L(p_i) - \mathbf{u}^L(p_i)\|}{\sigma_{k+1}} \right] \sqrt{\kappa \sigma_k^2 + \epsilon(\kappa)}. \tag{27}$$

This bound motivates the application of the multifidelity approximation due to the following reasons: (a) the error in the low-fidelity model $\|\hat{\mathbf{u}}^L(p_i) - \mathbf{u}^L(p_i)\|$ is small since it is reasonable to assume that the low-fidelity model is of low rank, and hence, the least squares approximation $\hat{\mathbf{u}}^L(p_i)$ (cf Equation (17)) is an accurate estimation of $\mathbf{u}^L(p_i)$; (b) in this bound, we need also some proximity assumption between low- and high-resolution Gramians similar to the analysis in

the work of Narayan et al.³³ to ensure small $\epsilon(\kappa)$. This assumption, however, is not a substantial practical limitation since it does *not* assume the proximity between the low- and high-resolution responses \mathbf{u}^L and \mathbf{u}^H themselves, which are possibly not proximal in practice. We note, however, that in the cases where responses \mathbf{u}^L and \mathbf{u}^H do converge to an asymptotic response u by means of refining the discretization (similar to the case in this paper), a recent analysis confirms that this multifidelity procedure is effective.³⁶

Having the above known theoretical guarantees, we proceed with deriving estimates for each compliance sample and its derivative. In other words, we show that the differences $|C(p_i) - \hat{C}(p_i)|$, $\|\partial C(p_i)/\partial \rho - \partial \hat{C}(p_i)/\partial \rho\|_2$, $\forall p_i \in \Gamma$ are bounded for an arbitrary iteration throughout the optimization. In most of our analyses, we do not show the dependence of these quantities on parameters and optimization iteration.

To derive an estimate for compliance, we first need to analyze the difference in the displacement approximations, ie, $\|\mathbf{u}^H - \hat{\mathbf{u}}^H\|_2$, which we adopt from the work of Narayan et al.³³ This difference is bounded via the triangle inequality

$$\|\mathbf{u}^H - \hat{\mathbf{u}}^H\| \leq \left\| \mathbf{u}^H - \mathbf{P}_{\mathbf{U}_{\Gamma_n}^H} \mathbf{u}^H \right\| + \left\| \mathbf{P}_{\mathbf{U}_{\Gamma_n}^H} \mathbf{u}^H - \hat{\mathbf{u}}^H \right\|, \quad (28)$$

where $\mathbf{P}_{\mathbf{U}_{\Gamma_n}^H}$ is the \mathbf{U}^H -orthogonal projector onto $\mathbf{U}_{\Gamma_n}^H$. The first term on the right-hand side is rather abstract and is typically bounded via a Kolmogorov n -width argument for the samples obtained from the greedy procedure (15), ie,

$$\sup_{p_i \in \Gamma} \left\| \mathbf{u}^H - \mathbf{P}_{\mathbf{U}_{\Gamma_n}^H} \mathbf{u}^H(p_i) \right\| \leq C_1 \sqrt{d_{n/2}(\mathbf{u}(\Gamma))}, \quad (29)$$

where $d_n(\mathbf{u}^H(\Gamma))$ is the n -width of the manifold $\mathbf{u}^H(\Gamma)$.³³ A detailed analysis of this term is beyond the scope of this work; however, we assume that the contribution of this error is negligible with respect to the second term on the right-hand side. This assumption is frequently true in practice, and therefore, we assume it to be a fraction of the second error term. This assumption will be verified in the numerical examples.

Now, let $\sqrt{\mathbf{G}^H} = \mathbf{V} \sqrt{\mathbf{S}} \mathbf{V}^T$ be the square root of the positive (semi)definite Gramian $\mathbf{G}^H = \mathbf{V} \sqrt{\mathbf{S}} \mathbf{V}^T$, where \mathbf{S} and \mathbf{V} are eigenvalues and eigenvectors, respectively, of \mathbf{G}^H . We need to formalize an assumption before proceeding.

Assumption 1. The low- and high-fidelity coefficients are close, ie,

$$\|\mathbf{c}^H - \mathbf{c}^L\| \leq \epsilon, \quad (30)$$

and the ratio

$$\delta = \frac{\left\| \mathbf{u}^H - \mathbf{P}_{\mathbf{U}_{\Gamma_n}^H} \mathbf{u}^H \right\|}{\left\| \mathbf{P}_{\mathbf{U}_{\Gamma_n}^H} \mathbf{u}^H - \hat{\mathbf{u}}^H \right\|} \quad (31)$$

is small, ie, $\delta \ll 1$.

The following lemma bounds the error in the displacement approximation (28).

Lemma 1. *Let n important samples be given via (15) and assumptions (30) and (31) hold, then*

$$\|\mathbf{u}^H - \hat{\mathbf{u}}^H\| \leq \epsilon(1 + \delta) \sqrt{\sigma_{\max}(\mathbf{G}^H)}, \quad (32)$$

where $\sigma_{\max}(\mathbf{G}^H)$ is the largest singular value of \mathbf{G}^H .

Proof. The second error on the right-hand side of (28) is expressed as

$$\begin{aligned} \left\| \mathbf{P}_{\mathbf{U}_{\Gamma_n}^H} \mathbf{u}^H - \hat{\mathbf{u}}^H \right\|^2 &= \left\| \sum_{j=1}^n (\mathbf{c}_j^H - \mathbf{c}_j^L) \mathbf{u}^H(p_j) \right\|^2 \\ &= (\mathbf{c}^H - \mathbf{c}^L) \mathbf{G}^H (\mathbf{c}^H - \mathbf{c}^L) = \left\| \sqrt{\mathbf{G}^H} (\mathbf{c}^H - \mathbf{c}^L) \right\|^2 \\ &\leq \left\| \sqrt{\mathbf{G}^H} \right\|^2 \|\mathbf{c}^H - \mathbf{c}^L\|^2 \leq \sigma_{\max}(\mathbf{G}^H) \epsilon^2, \end{aligned} \quad (33)$$

which yields $\|P_{U_{r_n}^H} \mathbf{u}^H - \hat{\mathbf{u}}^H\| \leq \epsilon \sqrt{\sigma_{\max}(\mathbf{G}^H)}$. Using this inequality and definition (31) in inequality (28) yields the estimate (32). \square

Remark 2. As mentioned, the ratio δ is not known a priori via analytical estimates. In practice, we directly compute it in our numerical experiments by using the first few unimportant high-resolution samples in the pivot vector and selecting the worst ratio, ie, the largest one. We also compute \mathbf{f}^H and subsequently \mathbf{c}^H associated with that particular unimportant sample and find an approximate value for ϵ .

The following proposition bounds the error for the compliance and its sensitivity.

Proposition 1. *Let the bifidelity approximation error in displacement be given by (32), then the error in compliance approximation and its sensitivity is bounded by*

$$\begin{aligned} |C - \hat{C}| &\leq A \sigma_{\max}(\mathbf{K}) \\ \left\| \frac{\partial C}{\partial \boldsymbol{\rho}} - \frac{\partial \hat{C}}{\partial \boldsymbol{\rho}} \right\| &\leq A \sigma_{\max} \left(\frac{\partial \mathbf{K}}{\partial \boldsymbol{\rho}} \right), \end{aligned} \quad (34)$$

where

$$A = \epsilon(1 + \delta) \sigma_{\max}(\mathbf{G}^H) [2\|\mathbf{c}^L\| + \epsilon(1 + \delta)], \quad (35)$$

σ_{\max} denotes the largest singular value, and \mathbf{K} , $\partial \mathbf{K} / \partial \boldsymbol{\rho}$ denote the global stiffness matrix (cf Equation (7)) and its derivative.

Proof. We use the result of Lemma 1 and the definition of compliance and its derivative, ie, $C = \mathbf{u}^T \mathbf{K} \mathbf{u}$, $\partial C / \partial \boldsymbol{\rho} = -\mathbf{u}^T (\partial \mathbf{K} / \partial \boldsymbol{\rho}) \mathbf{u}$:

$$\begin{aligned} |C - \hat{C}| &= \|\mathbf{u}^T \mathbf{K} \mathbf{u} - \hat{\mathbf{u}}^T \mathbf{K} \hat{\mathbf{u}}\| = \|(\mathbf{u}^T - \hat{\mathbf{u}}^T) \mathbf{K} \mathbf{u} + \hat{\mathbf{u}}^T \mathbf{K} (\mathbf{u} - \hat{\mathbf{u}})\| \\ &\leq \|\mathbf{u} - \hat{\mathbf{u}}\| \sigma_{\max}(\mathbf{K}) [\|\mathbf{u}\| + \|\hat{\mathbf{u}}\|] \\ &\leq \|\mathbf{u} - \hat{\mathbf{u}}\| \sigma_{\max}(\mathbf{K}) [\|\mathbf{u} - \hat{\mathbf{u}}\| + 2\|\hat{\mathbf{u}}\|]. \end{aligned} \quad (36)$$

According to (32) and (33), we have

$$\begin{aligned} \|\mathbf{u} - \hat{\mathbf{u}}\| &\leq \epsilon(1 + \delta) \sqrt{\sigma_{\max}(\mathbf{G}^H)} \\ \|\hat{\mathbf{u}}\| &= \left\| \sqrt{\mathbf{G}^H} \mathbf{c}^L \right\| \leq \sqrt{\sigma_{\max}(\mathbf{G}^H)} \|\mathbf{c}^L\|. \end{aligned} \quad (37)$$

Using the above estimates in (36) yields

$$\begin{aligned} |C - \hat{C}| &\leq \epsilon(1 + \delta) \sigma_{\max}(\mathbf{K}) \sigma_{\max}(\mathbf{G}^H) [\epsilon(1 + \delta) + 2\|\mathbf{c}^L\|] \\ &= A \sigma_{\max}(\mathbf{K}). \end{aligned} \quad (38)$$

Similarly, the bound for compliance sensitivity is obtained by replacing $\sigma_{\max}(\mathbf{K})$ with $\sigma_{\max}(\partial \mathbf{K} / \partial \boldsymbol{\rho})$ in the above estimate. \square

4 | NUMERICAL ILLUSTRATION

4.1 | Loading variability

In this example, we consider variations in loading on a square carrier plate shown in Figure 4. The domain is discretized using standard square FEs with different numbers of elements from coarse to fine meshes, ie, 4×4 , 10×10 , 20×20 , 50×50 , and 100×100 elements. We fix the top two layers of elements as solid elements to ensure the connectivity between load and structure. The load consists of a deterministic distributed vertical load $f_2 = 2$ and random horizontal load $f_1(x, p)$, which is modeled as a random field (cf Equation (12)) with zero mean and square exponential covariance function similarly to Equation (11) with $l_c = 0.2$. In Equation (12), we assume $\phi(\mathbf{p})$ as uniform random variables $U[-1, 1]$ and consider $n_M = 10$ modes, which yields the ratio $\sum_{i=1}^{10} \sqrt{\eta_i} / \sum_{i=1}^{100} \sqrt{\eta_i} = 0.9$, reasonably close to 1. The first five modes of loading are shown in Figure 5.

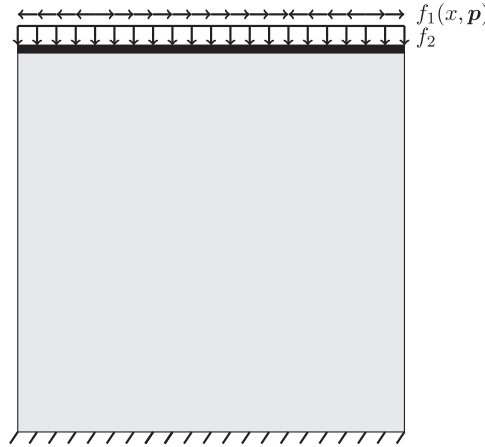


FIGURE 4 Carrier plate geometry for the simulation in Section 4.1

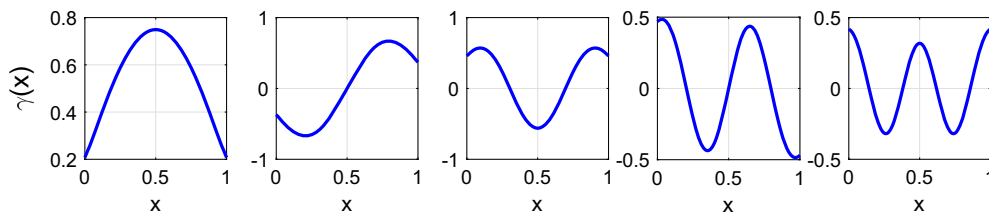


FIGURE 5 First five modes of Karhunen-Loeve expansion for loading [Colour figure can be viewed at wileyonlinelibrary.com]

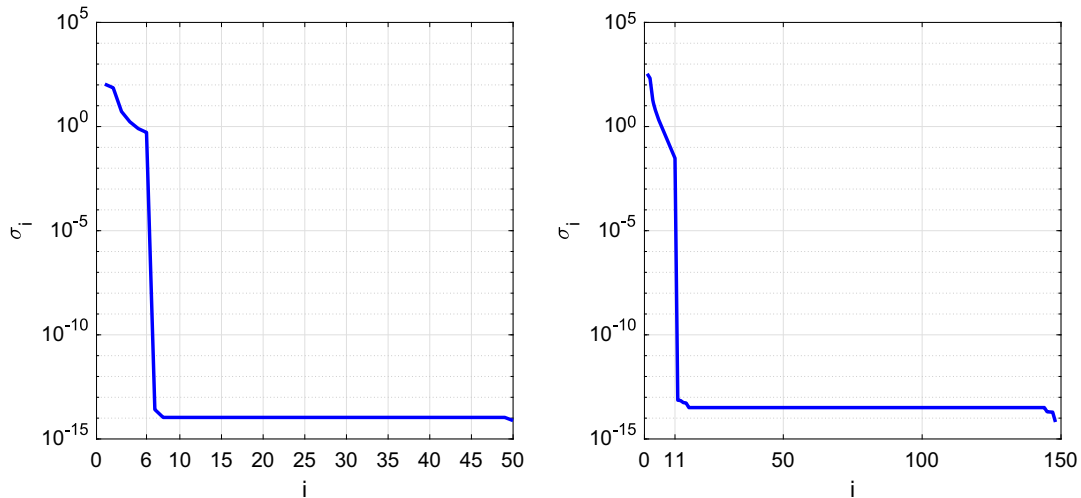


FIGURE 6 Decay of singular values in $\mathbf{u}^L(\Gamma_N)$ for 4×4 and 10×10 meshes [Colour figure can be viewed at wileyonlinelibrary.com]

To apply these modal loads on the structure with lower resolution, we simply interpolate the high-resolution modes, eg, the ones with 100 elements (shown in Figure 5). To compute statistical moments, we compute discretizations to the corresponding integrals using the technique of *designed quadrature*, which was developed previously by the authors.³⁷ This quadrature rule is specially designed for integration in multiple dimensions where the positivity of weights is ensured and, in all cases, tested that the number of nodes is smaller than that in a corresponding sparse grid rule. We use $N = 148$ points that integrate a function with 10 variables associated with n_M in (12) and the total order $\alpha = 5$, ie, this set of points can integrate $\int x_1^{\alpha_1} x_2^{\alpha_2} \dots x_{10}^{\alpha_{10}} dx_1 dx_2 \dots dx_{10}$ for $\sum_{i=1}^{10} \alpha_i \leq 5$ accurately. We deem the total order $\alpha = 5$ sufficient for our problem.

The next two Figures show some intermediate results associated with an iteration in the middle of optimization. Figure 6 shows the decay of singular values in the low-resolution models $\mathbf{u}^L(\Gamma_N)$ for 4×4 and 10×10 meshes. As seen, the coarser mesh has only numerical rank $r = 6$, whereas the finer mesh has $r = 11$. This suggests that all 10 horizontal modes and

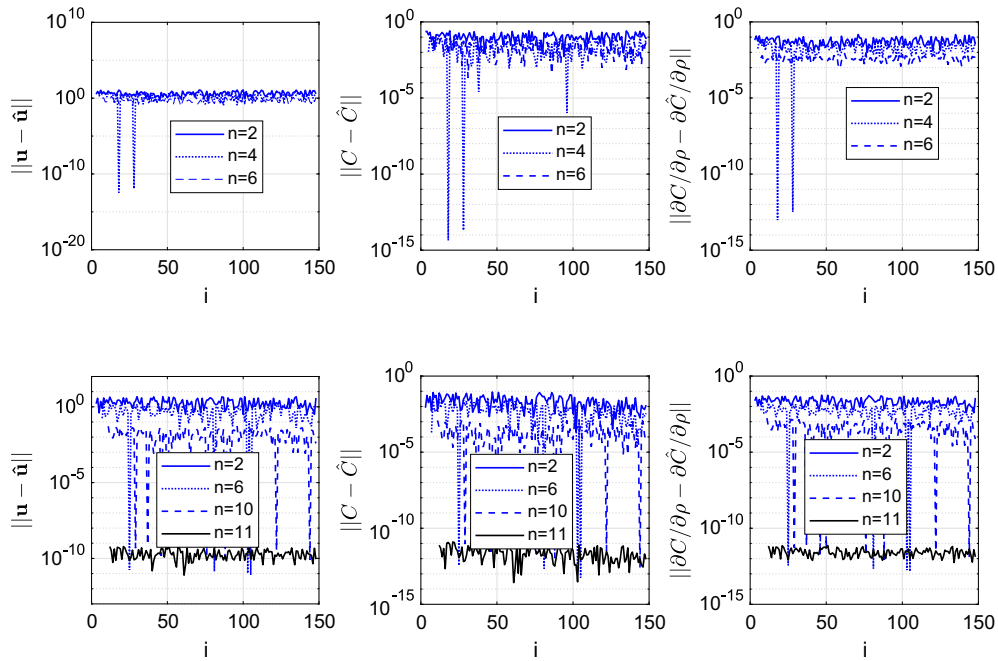


FIGURE 7 Bifidelity actual approximation error for displacement, compliance, and compliance sensitivity with respect to different numbers of high-resolution simulations n for 4×4 (top) and 10×10 (bottom) meshes [Colour figure can be viewed at wileyonlinelibrary.com]

the vertical load can be captured by the finer mesh whereas the coarser one does not have enough degrees of freedom (DOFs; only 6) to capture all modal loads.

Figure 7 shows the difference between bifidelity approximation and high-fidelity solutions for the displacement, compliance, and compliance sensitivity with respect to different values on n , number of high-resolution simulations.

Topology optimization results with different meshes are plotted in Figure 8. We use filter radius values $r_{\min} = 6, 3, 2, 1.5, 1.05$, respectively, for our five different mesh sizes. (See the caption of Figure 8 for these mesh sizes.) In the case of the two coarsest meshes, 4×4 and 10×10 , we only fix the top layer instead of the top two layers. We use the same optimality criteria algorithm^{27,38} to update the design parameters until the optimization converges. From these plots, it is obvious that the single-resolution optimizations (top plots) with coarse meshes yield uninformative topology designs, but using these coarse meshes in our biresolution framework results in designs that are almost identical to high-resolution optimization.

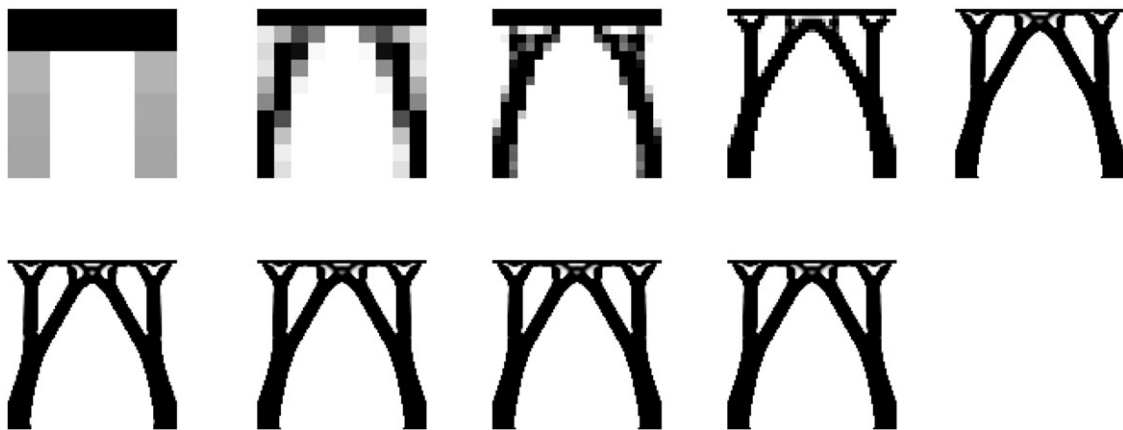
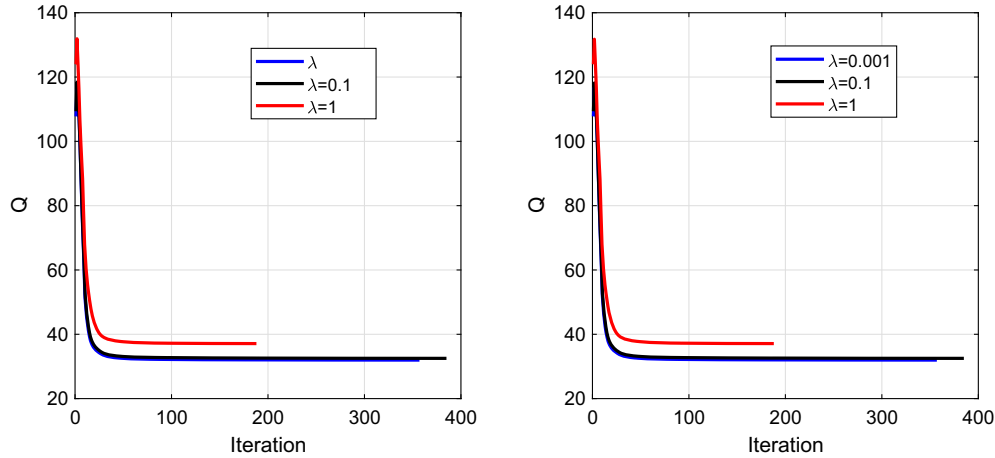
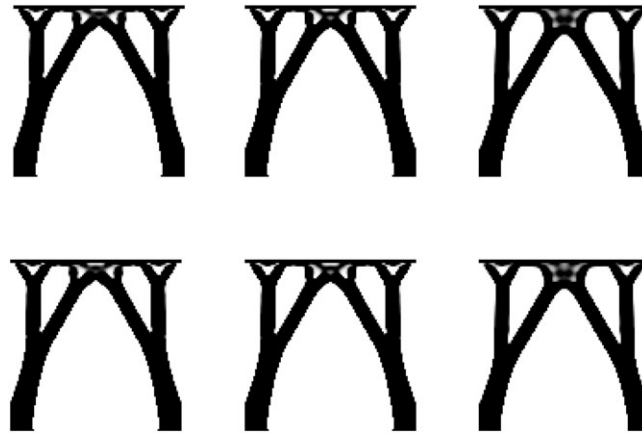


FIGURE 8 Topology optimization results for different meshes: single-resolution optimization with 4×4 , 10×10 , 20×20 , 50×50 , and 100×100 meshes (top row) and bifidelity optimization with 4×4 , 10×10 , 20×20 , and 50×50 meshes (bottom row). The top-right figure is obtained with 148 high-resolution simulations (on a 100×100 mesh) at each design iteration, whereas the bottom plots associated with 10×10 , 20×20 , and 50×50 meshes are obtained with only 11 high-resolution simulations. The bottom-left plot associated with a 4×4 mesh is obtained with six high-resolution simulations

TABLE 1 Loading uncertainty: error vs cost for single-resolution and biresolution optimizations

Resolution	No. Iter.	No. Hi. Res. Sim.	e_ρ	e_Q
Hi. Res. 100×100	385	56 980	–	–
Bi-Res. 4×4	587	3522	$1.09\text{e-}01$	$2.32\text{e-}02$
Bi-Res. 10×10	385	4235	$5.74\text{e-}05$	$2.01\text{e-}05$
Bi-Res. 20×20	385	4235	$5.74\text{e-}05$	$2.01\text{e-}05$
Bi-Res. 50×50	385	4235	$5.74\text{e-}05$	$2.01\text{e-}05$

**FIGURE 9** Effect of λ on optimized objective function Q . Left and right figures are obtained from single high-resolution 100×100 optimization and bifidelity optimization with a 10×10 mesh, respectively [Colour figure can be viewed at wileyonlinelibrary.com]**FIGURE 10** Effect of λ on optimal design: $\lambda = 0.001$ (left), $\lambda = 0.1$ (middle), and $\lambda = 1$ (right). Top and bottom figures are obtained from single high-resolution 100×100 optimization and bifidelity optimization with a 10×10 mesh, respectively

We compute the difference between optimal designs obtained from the biresolution approach and high-resolution design as $e_\rho = \|\rho^B - \rho^H\| / \sqrt{n_{\text{elem}}^H}$, where $n_{\text{elem}}^H = 10^4$ in this case. Similarly, we define the error in the objective function Q (cf Equation (9)) as $e_Q = |Q^B - Q^H| / Q^H$. Table 1 shows the number of iterations; the number of high-resolution simulations, which is 6 for the coarsest mesh and 11 for the rest of the meshes at each iteration; and e_ρ and e_Q . It is apparent that the biresolution topology optimization with a 10×10 mesh yields almost the same design with much smaller cost.

To investigate the effect of standard deviation weight on the optimal design, we consider three values for $\lambda = 0.001, 0.1, 1$ (cf Equation (9)). Figure 9 shows the optimization iteration for both single-resolution and biresolution optimizations, which are almost identical for different values of λ . We show the corresponding designs in Figure 10, where, again, similar topologies are obtained.

TABLE 2 Actual error vs upper-bound estimate. Estimated values are computed as the bounding certificates in Lemma 1 and Proposition 1

	$\ \mathbf{u} - \hat{\mathbf{u}}\ $	$ \mathbf{C} - \hat{\mathbf{C}} $	$\ \partial\mathbf{C}/\partial\rho_1 - \partial\hat{\mathbf{C}}/\partial\rho_1\ $
Actual	3.64e-07	1.57e-08	3.18e-09
Estimate	5.76e-05	3.26e-04	3.33e-04

Finally, we compute the error bound in approximation of displacement, compliance, and compliance sensitivity. To that end, we consider the first iteration where the densities are considered uniformly $\rho = 0.35$. We also consider $n = 11$ with a 10×10 mesh as the full rank of the low-fidelity model. As mentioned earlier, to obtain δ , we directly compute the two norms in (28) for the first few unimportant samples. The maximum ratio is computed to be $\delta = 0.916$ for the third sample after $n = 11$ samples. The maximum norm for the stiffness matrix and its derivative with respect to the first design variable (the element in the bottom-left corner) are $\sigma_{\max}(\mathbf{K}) = 1.0476$ and $\sigma_{\max}(\partial\mathbf{K}/\partial\rho_1) = 1.0714$. We have also computed $\sigma_{\max}(\mathbf{G}^H) = 113.384$ and $\epsilon = 2.825e - 06$ directly from the high-fidelity data. The actual and estimated errors for the aforementioned sample are listed in Table 2.

From this single point, it is evident that the upper bound is relatively small. The actual error for a bifidelity surrogate is even smaller, which promises almost identical designs for parametric topology optimization, as evidenced by Figure 8.

4.2 | Manufacturing tolerances

In this example, we consider uncertainty in the thresholding parameter τ (cf Equation (6)) to mimic the geometric variations in the thickness of resulting truss bars in the L-shape domain shown in Figure 11. We use $l_c = 0.85$ in Equation (11), which results in $\sum_{i=1}^4 \sqrt{\eta_i} / \sum_{i=1}^{100} \sqrt{\eta_i} = 0.88$. We also use $N = 43$ designed quadrature points that integrate $d = 4$ dimensions with order $\alpha = 6$ accurately.³⁷ The $n_M = 4$ Karhunen-Loeve modes and four realizations of spatial threshold $\tau = 0.1Z + 0.45$ corresponding to arbitrary quadrature nodes are shown in Figure 12.

Similarly to loading uncertainty, we consider different numbers of high-resolution simulations n in the bifidelity construction and show the difference between bifidelity approximation and high-fidelity solutions for the displacement, compliance, and compliance sensitivity (cf Figure 13). Again, as expected, as the number of high-resolution simulations increases, more accurate bifidelity approximations are obtained.

We use filter radius $r_{\min} = 6, 3, 2.5, 2, 1.5$ for different meshes in this case and set $\lambda = 0.1$. Topology optimization results for single-resolution and bi-resolution models are shown in Figure 14. In the bi-resolution optimizations, only 10 high-resolution simulations are performed, whereas single-resolution optimization is performed with 43 simulations.

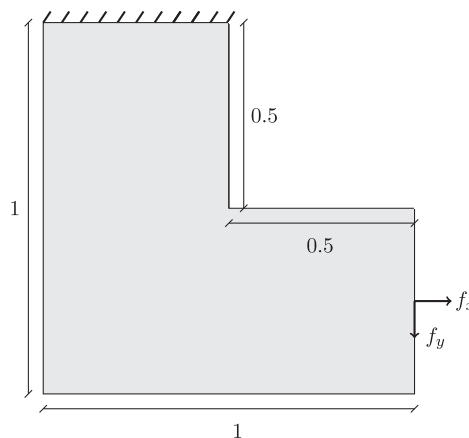


FIGURE 11 L-bracket geometry for the simulation in Section 4.2

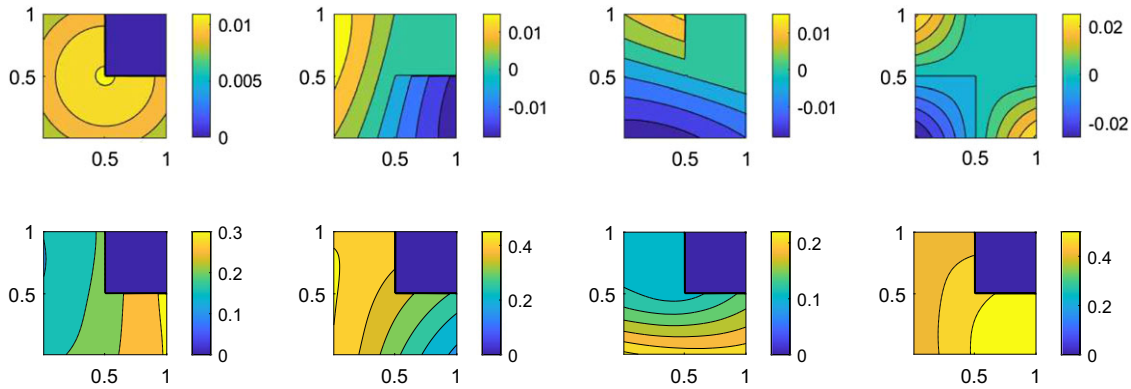


FIGURE 12 Karhunen-Loeve modes for the spatial random field (top) and different realizations of the spatial threshold on quadrature points (bottom) [Colour figure can be viewed at wileyonlinelibrary.com]

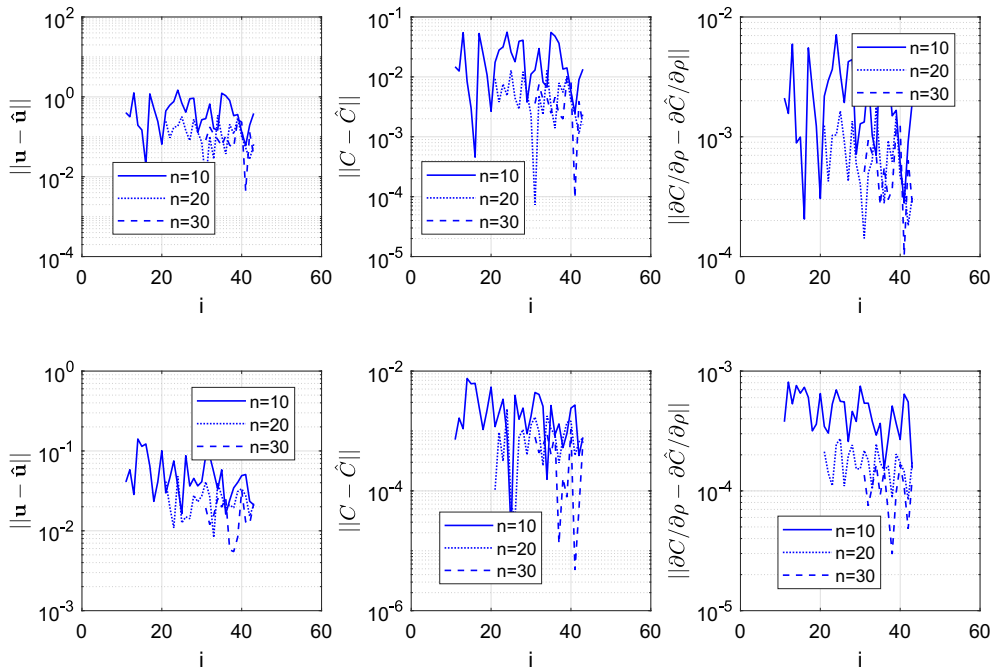


FIGURE 13 Bifidelity actual approximation error for displacement, compliance, and compliance sensitivity with respect to different numbers of high-resolution simulations n for 4×4 (top) and 10×10 (bottom) meshes [Colour figure can be viewed at wileyonlinelibrary.com]

To quantify the differences between single-resolution and biresolution optimizations, we perform the same study as done in the previous example. Table 3 shows the error versus the cost for single-resolution and biresolution optimizations. We again observe that a 10×10 mesh is the most economical choice as it yields the small error, whereas most of the computation is performed on its relatively coarse mesh.

As mentioned, the processed design variables $\bar{\rho}$ are random due to the randomness in τ . We define the error in the mean and standard deviation of processed design variables between single-resolution and biresolution models as $e_{\mu(\bar{\rho})} = \|\mu(\bar{\rho}^B) - \mu(\bar{\rho}^H)\| / \sqrt{n_{\text{elem}}^H}$ and $e_{\sigma(\bar{\rho})} = \|\sigma(\bar{\rho}^B) - \sigma(\bar{\rho}^H)\| / \sqrt{n_{\text{elem}}^H}$, which are computed as $e_{\mu(\bar{\rho})} = 2.75e - 03$ and $e_{\sigma(\bar{\rho})} = 1.86e - 03$. Figure 15 shows the mean and standard variation for the processed design variables obtained from single-resolution and biresolution optimizations.

Now that we can obtain high-fidelity compliance values efficiently, we perform a more challenging RBDO (cf Equation (10)), where we set $\bar{C} = 500$, $\delta_{p_j} = 0.05$. We use the *method of moving asymptotes*³⁹ to solve this optimization problem and consider $N = 1000$ biresolution MC samples with $n = 10$ to compute the probability of failure and its sensitivity at each design iterate. This means we perform $n = 10$ high-resolution FEA and $N = 1000$ low-resolution FEA to find biresolution approximations. The optimized topology is shown in Figure 16. To investigate the accuracy, we perform

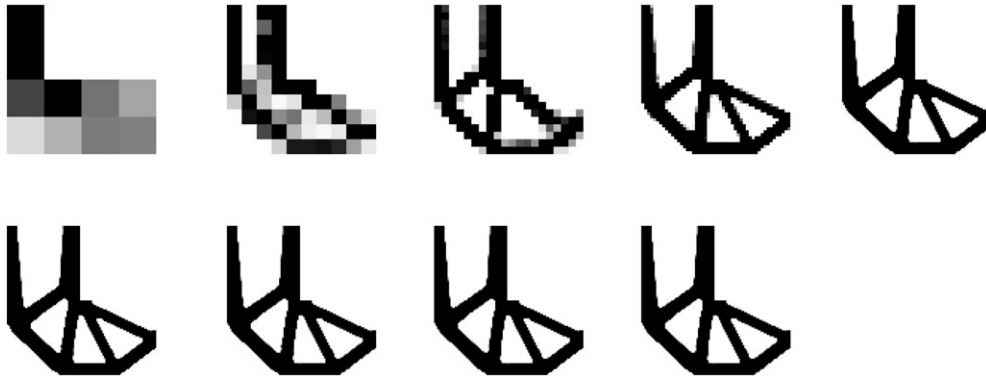


FIGURE 14 Topology optimization results for different meshes and $\lambda = 0.1$: single-resolution optimization with 4×4 , 10×10 , 20×20 , 50×50 , and 100×100 meshes (top row); bifidelity optimization with 4×4 , 10×10 , 20×20 , and 50×50 meshes (bottom row). All biresolution results are obtained with 10 high-resolution simulations, which are almost identical to the top-right plot that uses 43 simulations at each design iterate

TABLE 3 Geometric uncertainty: error vs cost for single-resolution and biresolution optimizations

Resolution	No. Iter.	No. Hi. Res. Sim.	e_ρ	e_Q
Hi. Res. 100×100	240	10 320	–	–
Bi-Res. 4×4	283	2830	0.0236	$4.24e-03$
Bi-Res. 10×10	276	2760	0.0155	$1.51e-04$
Bi-Res. 20×20	268	2680	0.0130	$1.29e-04$
Bi-Res. 50×50	255	2550	0.0093	$9.10e-05$

$N = 10^4$ high-resolution MC and $N = 10^4$ biresolution MC with $n = 10$ on the final design to generate compliance probability density functions and CDFs. The probability of failure for high-resolution and biresolution analyses is estimated as $\Pr[C > \bar{C}] = 0.048, 0.047$, which are reasonably close to each other and to the limit $\delta_{p_f} = 0.05$.

Finally, to show the effectiveness of our approach in approximating challenging quantities of interest, we compute the parametric von Mises stress for the optimal design using the biresolution approach and compare it with MC and multi-level Monte Carlo (MLMC) simulations.⁴⁰ Figure 17 shows a realization of high- and low-resolution von Mises stresses associated with 100×100 and 10×10 meshes on one of 43 quadrature points. It is again observed that the low-resolution mesh provides no insight on stress distribution; however, by using it in the biresolution framework in conjunction with 10 high-resolution stress distribution samples, we can approximate the rest of the 33 high-resolution stresses.

We use the biresolution quadrature samples to compute the mean and standard deviation of spatially averaged stresses. In addition, we perform 1000 high-resolution MC simulations (associated with 1000 samples of the threshold random field; cf Equation (12)) to find the mean and standard deviation of the same quantity of interest. For MLMC approximation, we use $n = 10$ high-resolution and $N = 1000$ low-resolution samples to compute the mean and standard deviation via the multilevel strategy. That is, we compute

$$\begin{aligned}
 E_{\text{MLMC}}[Q] &= E_L[Q^L] + E_H[Q^H - Q^L] \\
 E_{\text{MLMC}}[Q^2] &= E_L[Q^{L^2}] + E_H[Q^{H^2} - Q^{L^2}] \\
 \sigma_{\text{MLMC}} &= \sqrt{E_{\text{MLMC}}[Q^2] - \mu_{\text{MLMC}}^2},
 \end{aligned} \tag{39}$$

where $\mu_{\text{MLMC}} = E_{\text{MLMC}}[Q]$ and E_L and E_H are sample averages with 1000 and 10 samples, respectively. That is, to compute $E_H[Q^H - Q^L]$, we use 10 high-resolution samples as well as 10 low-resolution samples (corresponding to the same parametric values). On the other hand, to compute $E_L[Q^L]$, we generate 10^3 low-resolution samples inexpensively and find their sample average. To investigate the error, we use a high-level sparse grid with $n = 1217$ nodes as the true solution.⁴¹ Figure 18 shows the convergence of the MC simulations and the error between the biresolution approximation and the true solution as well as the MLMC approximation and the true solution. It is seen that the biresolution approximation of stress with only 10 high-resolution simulations outperforms MC simulations with a much larger number of high-resolution simulations and MLMC approximations. It is also worth mentioning that MLMC methods are only



FIGURE 15 Mean (left) and standard deviation (right) of processed design variables $\bar{\rho}$ obtained from biresolution optimization with a 10×10 mesh (top) and single-resolution optimization of a 100×100 mesh (bottom)

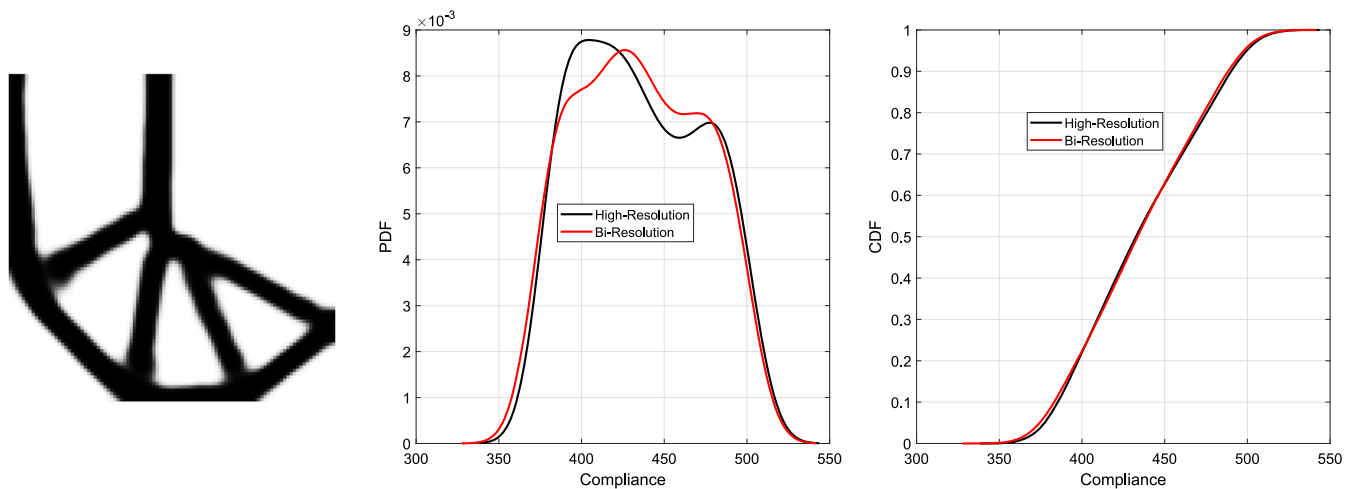


FIGURE 16 A nominal reliability-based design using the biresolution approximation (left), probability density functions (PDFs; middle), and cumulative distribution functions (CDFs; right) of compliance obtained via high-resolution and biresolution finite element analyses [Colour figure can be viewed at wileyonlinelibrary.com]

applicable to problems where the approximation of statistical moments is concerned, eg, RDO problems, whereas our biresolution strategy is a systematic tool to generate high-fidelity samples that can be used in RBDO problems, which require a large number of high-fidelity samples (as shown in Figure 16).

4.3 | Three-dimensional topology optimization

In order to demonstrate the effectiveness of our approach in reducing computational cost, we consider three-dimensional (3D) topology optimization in the last example. Figure 19 shows the geometry and boundary conditions of the problem. The middle of the beam is subjected to a random vertical load similarly to the shear load in Example 4.1. We use the symmetry and optimize half of the structure where we fix the x and z DOFs associated with the nodes in the middle plane as well as the y DOFs associated with the nodes in the lower-right corner along the z -direction. The high- and low-resolution FEAs consist of $60 \times 20 \times 10$ and $24 \times 8 \times 4$ brick elements with 42 273 and 3375 DOFs, respectively. This

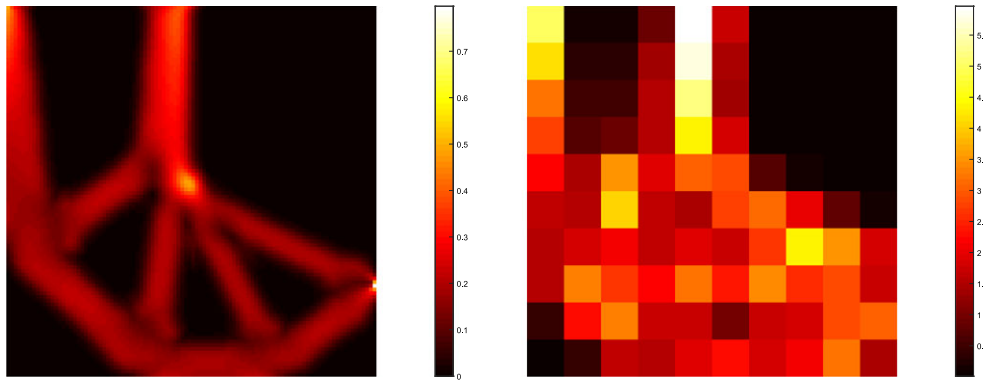


FIGURE 17 A realization of high- and low-resolution von Mises stresses associated with 100×100 and 10×10 meshes [Colour figure can be viewed at wileyonlinelibrary.com]

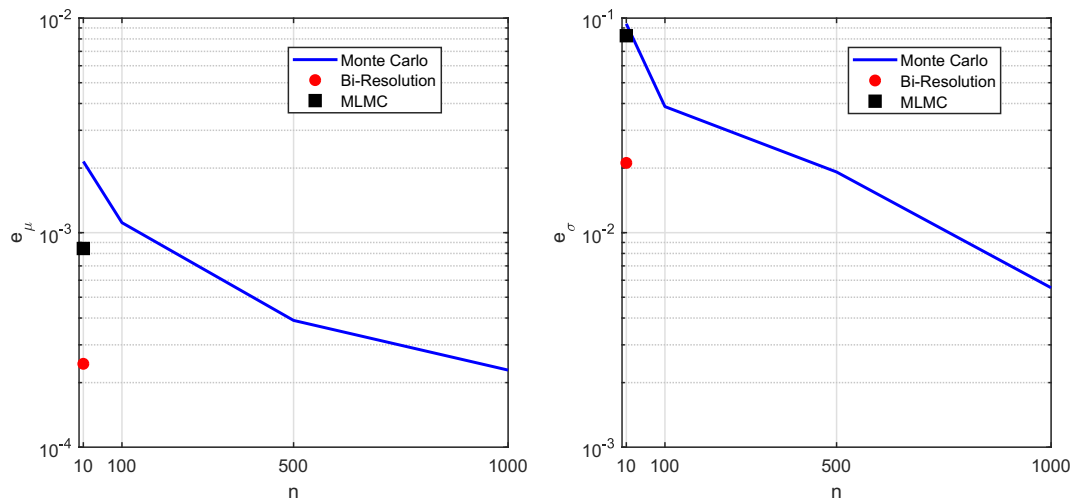


FIGURE 18 Error in mean (left) and standard deviation (right) of spatially averaged von Mises stress. The abscissa n is the number of high-resolution simulations. MLMC, multilevel Monte Carlo [Colour figure can be viewed at wileyonlinelibrary.com]

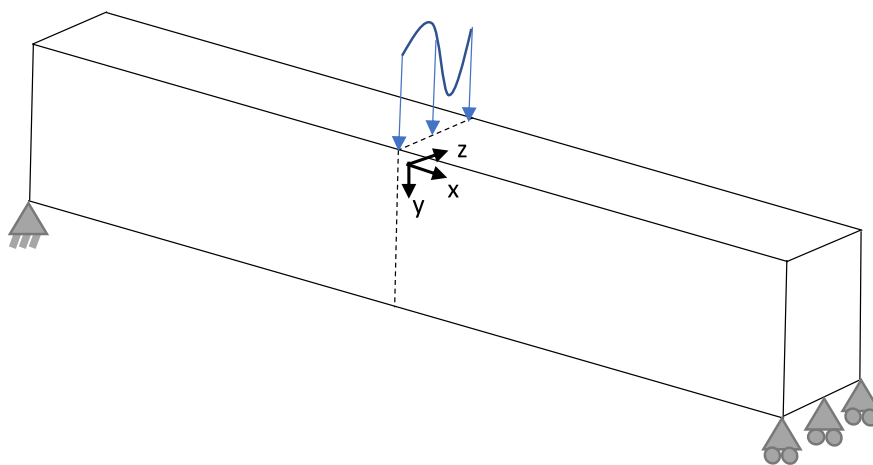


FIGURE 19 Geometry and boundary condition for a three-dimensional linear elastic structure for simulations in Section 4.3 [Colour figure can be viewed at wileyonlinelibrary.com]

results in a 92% reduction ($1 - (3375/42273) = 0.92$) in DOFs in low-resolution analyses, which drastically decreases the computational complexity of linear solves in parametric computations. We took advantage of the MATLAB code provided in the work of Liu and Tovar⁴² for 3D FE computations and part of the code provided in the work of Zegard and Paulino⁴³

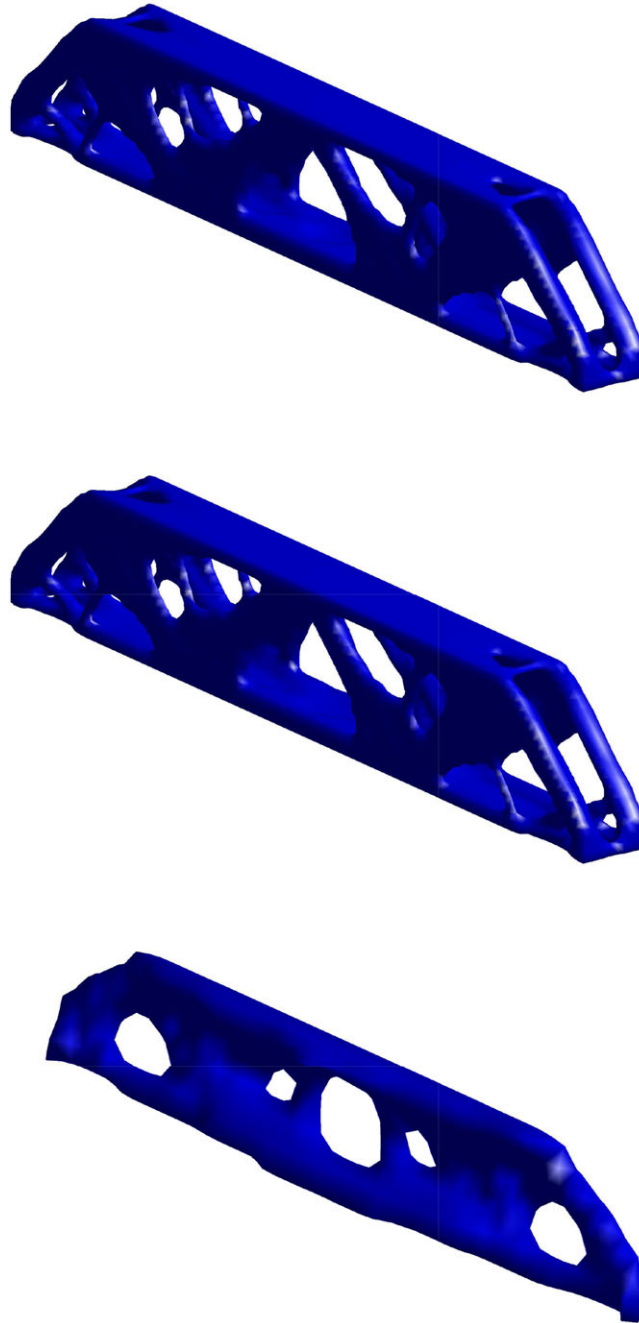


FIGURE 20 Optimized topology for a three-dimensional linear elastic beam using high-resolution approximations (top), bi-resolution approximations (middle), and low-resolution approximations (bottom) [Colour figure can be viewed at wileyonlinelibrary.com]

for visualization of 3D designs. We solve the RDO problem (cf Equation (9)) with $\lambda = 0.1$ and use $n = 5$ high-resolution and $N = 500$ low-resolution simulations throughout the optimization. Figure 20 shows the optimized designs associated with high-resolution, bi-resolution, and low-resolution approximations. It is apparent that there is no significant difference between high-resolution and bi-resolution robust designs, whereas the low-resolution design is again uninformative by itself. Similar to the previous example, to investigate the accuracy of our approach, we compute the compliance probability density functions associated with two high-resolution and bi-resolution designs using 10^4 MC samples (cf Figure 21). The difference with the previous example is that we perform high-fidelity MC analyses on the first two designs in Figure 20, whereas in the previous example, we performed high-fidelity and bifidelity MC analyses on the final bifidelity design. The mean and standard deviation of compliance for these designs are $\mu = 212.00, \sigma = 28.24$ and $\mu = 210.41, \sigma = 27.74$, which are again deemed sufficiently close considering significant reduction in FE computations.

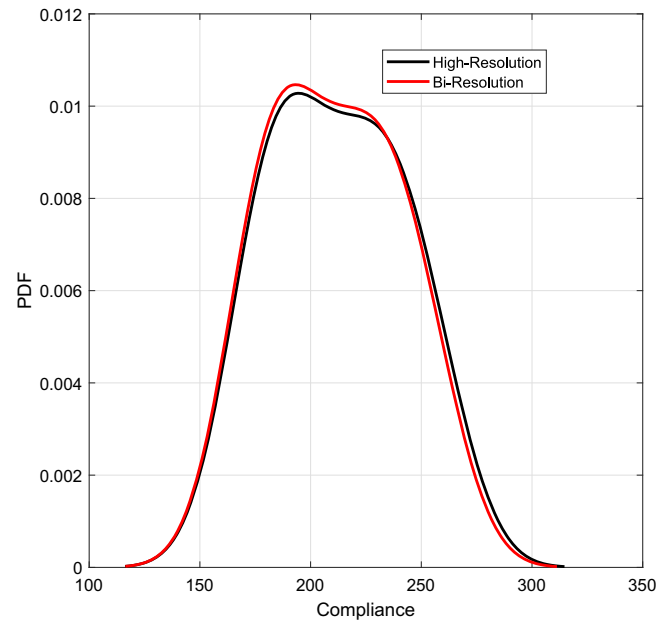


FIGURE 21 Compliance probability density functions (PDFs) for a three-dimensional optimized structure associated with high-resolution and bi-resolution robust designs [Colour figure can be viewed at wileyonlinelibrary.com]

5 | CONCLUSION

We have presented a systematic approach for parametric topology optimization with multiresolution FE models. The parametric variation is identified from an inexpensive low-resolution model, where a large number of simulations can be performed. The identified links among low-resolution samples are used to approximate the high-resolution parameter space, which now only requires a limited number of high-fidelity simulations. We use the bifidelity surrogate of displacement for compliance-based topology optimization on benchmark problems with loading and geometric variabilities. An error estimate for bifidelity approximation of compliance is derived, which certifies the convergence of approach. Numerical results are provided to delineate the convergence analysis. It is shown that the bi-resolution approach yields almost identical design to single-resolution optimization with significantly smaller computational cost especially in expensive problems, such as topology optimization under manufacturing uncertainty, reliability-based topology optimization, and 3D topology optimization.

ACKNOWLEDGEMENTS

This research was sponsored by the Army Research Laboratory (ARL) under Cooperative Agreement Number W911NF-12-2-0023. The first and third authors were partially supported by the Air Force Office of Scientific Research under grant FA9550-15-1-0467. The third author was partially supported by the Defense Advanced Research Projects Agency through the Enabling Quantification of Uncertainty in Physical Systems (EQUiPS) program under grant N660011524053 and the National Science Foundation Division of Mathematical Sciences under grant 1720416. The views and conclusions contained in this document are those of the authors and should not be interpreted as representing the official policies, either expressed or implied, of ARL or the US Government. The US Government is authorized to reproduce and distribute reprints for Government purposes notwithstanding any copyright notation herein.

ORCID

Vahid Keshavarzzadeh  <https://orcid.org/0000-0001-6685-9158>

REFERENCES

1. Bendsoe M, Kikuchi N. Generating optimal topologies in structural design using a homogenization method. *Comput Methods Appl Mech Eng*. 1988;71(2):197-224.

2. Sigmund O, Torquato S. Design of materials with extreme thermal expansion using a three-phase topology optimization method. *J Mech Phys Solids*. 1997;45(6):1037-1067.
3. Alexandersen J, Sigmund O, Meyer KE, Lazarov BS. Design of passive coolers for light-emitting diode lamps using topology optimisation. *Int J Heat Mass Transf*. 2018;122:138-149.
4. Dilgen SB, Dilgen CB, Fuhrman DR, Sigmund O, Lazarov BS. Density based topology optimization of turbulent flow heat transfer systems. *Struct Multidiscip Optim*. 2018;57(5):1905-1918.
5. Lundgaard C, Sigmund O. A density-based topology optimization methodology for thermoelectric energy conversion problems. *Struct Multidiscip Optim*. 2018;57(4):1427-1442.
6. Behrou R, Maute K. Multiscale modeling of non-local damage evolution in lithium-ion batteries. *ECS Transactions*. 2017;77(11):1163-1177.
7. Behrou R, Lawry M, Maute K. Level set topology optimization of structural problems with interface cohesion. *Int J Numer Methods Eng*. 2017;112(8):990-1016.
8. Martínez-Frutos J, Herrero-Pérez D, Kessler M, Periago F. Robust shape optimization of continuous structures via the level set method. *Comput Meth Appl Mech Eng*. 2016;305:271-291.
9. Allaire G, Dapogny C. A deterministic approximation method in shape optimization under random uncertainties. *J Comput Math*. 2015;1:83-143.
10. de Gournay F, Allaire G, Jouve F. Shape and topology optimization of the robust compliance via the level set method. *ESAIM Control Optimisation Calc Var*. 2008;1:43-70.
11. Keshavarzzadeh V, Meidani H, Tortorelli DA. Gradient based design optimization under uncertainty via stochastic expansion methods. *Comput Meth Appl Mech Eng*. 2016;306:47-76.
12. Keshavarzzadeh V, Fernandez F, Tortorelli DA. Topology optimization under uncertainty via non-intrusive polynomial chaos expansion. *Comput Meth Appl Mech Eng*. 2017;318:120-147.
13. Kang Z, Wu C, Luo Y, Li M. Robust topology optimization of multi-material structures considering uncertain graded interface. *Compos Struct*. 2019;208:395-406.
14. Zhang X, He J, Takezawa A, Kang Z. Robust topology optimization of phononic crystals with random field uncertainty. *Int J Numer Methods Eng*. 2018;115(9):1154-1173.
15. Torii AJ, Lopez RH, Miguel LFF. A gradient-based polynomial chaos approach for risk and reliability-based design optimization. *J Braz Soc Mech Sci Eng*. 2017;39(7):2905-2915.
16. Martínez-Frutos J, Herrero-Pérez D, Kessler M, Periago F. Risk-averse structural topology optimization under random fields using stochastic expansion methods. *Comput Meth Appl Mech Eng*. 2018;330:180-206.
17. da Silva GA, Beck AT. Reliability-based topology optimization of continuum structures subject to local stress constraints. *Struct Multidiscip Optim*. 2017;57(6):2339-2355.
18. Nguyen TH, Paulino GH, Song J, Le CH. A computational paradigm for multiresolution topology optimization (MTOP). *Struct Multidiscip Optim*. 2010;41(4):525-539.
19. Park J, Sutradhar A. A multi-resolution method for 3D multi-material topology optimization. *Comput Meth Appl Mech Eng*. 2015;285 (Supplement C):571-586.
20. Filipov ET, Chun J, Paulino GH, Song J. Polygonal multiresolution topology optimization (PolyMTOP) for structural dynamics. *Struct Multidiscip Optim*. 2016;53(4):673-694.
21. Kim YY, Yoon GH. Multi-resolution multi-scale topology optimization – a new paradigm. *Int J Solids Struct*. 2000;37(39):5529-5559.
22. Wang H, Fan T, Li G. Reanalysis-based space mapping method, an alternative optimization way for expensive simulation-based problems. *Struct Multidiscip Optim*. 2017;55(6):2143-2157.
23. Razi M, Narayan A, Kirby RM, Bedrov D. Fast predictive models based on multi-fidelity sampling of properties in molecular dynamics simulations. *Comput Mater Sci*. 2018;152:125-133.
24. Jones BA, Weisman R. Multi-fidelity orbit uncertainty propagation. *Acta Astronautica*. 2018;155:406-417.
25. Munipalli R, Hamilton J, Zhu X. A multifidelity approach to parameter dependent modeling of combustion instability. Paper presented at: 2018 Joint Propulsion Conference, AIAA Propulsion and Energy Forum; 2018; Cincinnati, OH.
26. Jofre L, Geraci G, Fairbanks H, Doostan A, Iaccarino G. Multi-fidelity uncertainty quantification of irradiated particle-laden turbulence. 2018. ArXiv Preprint, ArXiv:180106062.
27. Andreassen E, Clausen A, Schevenels M, Lazarov BS, Sigmund O. Efficient topology optimization in MATLAB using 88 lines of code. *Struct Multidiscip Optim*. 2011;43(1):1-16.
28. Keshavarzzadeh V. Parametric topology optimization with multi-resolution finite element models. <https://github.com/vahid28k/Parametric-TOPOPT-Multi-Resolution>
29. Bruns TE, Tortorelli DA. Topology optimization of non-linear elastic structures and compliant mechanisms. *Comput Meth Appl Mech Eng*. 2001;190(26-27):3443-3459.
30. Bendsøe MP. Optimal shape design as a material distribution problem. *Structural Optimization*. 1989;1(4):193-202.
31. Bendsøe MP, Sigmund O. Material interpolation schemes in topology optimization. *Arch Appl Mech*. 1999;69(9-10):635-654.
32. Hesthaven JS, Rozza G, Stamm B. *Certified Reduced Basis Methods for Parametrized Partial Differential Equations*. Cham, Switzerland: Springer International Publishing; 2016. *Springer Briefs in Mathematics*. <http://link.springer.com/10.1007/978-3-319-22470-1>
33. Narayan A, Gittelsohn C, Xiu D. A stochastic collocation algorithm with multifidelity models. *SIAM J Sci Comput*. 2014;36(2):495-521.

34. Golub GH, Van Loan CF. *Matrix Computations*. Baltimore, MD: Johns Hopkins University Press; 1996. *Johns Hopkins Studies in the Mathematical Sciences*.
35. Hampton J, Fairbanks HR, Narayan A, Doostan A. Practical error bounds for a non-intrusive bi-fidelity approach to parametric/stochastic model reduction. *J Comput Phys*. 2018;368:315-332.
36. Keshavarzzadeh V, Kirby RM, Narayan A. Convergence acceleration for time dependent parametric multifidelity models. 2018. ArXiv Preprint, ArXiv:180803379.
37. Keshavarzzadeh V, Kirby RM, Narayan A. Numerical integration in multiple dimensions with designed quadrature. *SIAM J Sci Comput*. 2018;40(4):A2033-A2061.
38. Bendsøe MP, Sigmund O. *Topology Optimization: Theory, Methods and Applications*. Berlin, Germany: Springer-Verlag Berlin Heidelberg; 2003.
39. Svanberg K. The method of moving asymptotes—a new method for structural optimization. *Int J Numer Methods Eng*. 1987;24(2):359-373.
40. Giles MB. Multilevel Monte Carlo methods. *Acta Numerica*. 2015;259-328. <https://www.cambridge.org/core/journals/acta-numerica/article/multilevel-monte-carlo-methods/C5AF9A57ED8FF8FDF08074C1071C5511>
41. Heiss F, Winschel V. Quadrature on sparse grids. <http://www.sparse-grids.de/>
42. Liu K, Tovar A. An efficient 3D topology optimization code written in Matlab. *Struct Multidiscip Optim*. 2014;50(6):1175-1196.
43. Zegard T, Paulino GH. Bridging topology optimization and additive manufacturing. *Struct Multidiscip Optim*. 2016;53(1):175-192.

How to cite this article: Keshavarzzadeh V, Kirby RM, Narayan A. Parametric topology optimization with multiresolution finite element models. *Int J Numer Methods Eng*. 2019;1–23. <https://doi.org/10.1002/nme.6063>